Available online at www.sciencedirect.com
ScienceDirect
Ceramics International 37 (2011) 2631–2641
CERAMICS INTERNATIONAL
www.elsevier.com/locate/ceramint

Development of hard/soft ferrite nanocomposite for enhanced microwave absorption

Sachin Tyagi [a,*], Himanshu B. Baskey [b], Ramesh Chandra Agarwala [a], Vijaya Agarwala [a], Trilok Chand Shami [b]

[a] Department of Metallurgical and Materials Engineering, Indian Institute Of Technology, Roorkee 247667, India
[b] Special Materials Group, DMSRDE (DRDO Lab) Kanpur, Uttar Pradesh, India

Received 15 March 2011; received in revised form 6 April 2011; accepted 7 April 2011
Available online 17 April 2011

Abstract

Nickel and zinc substituted strontium hexaferrite, $SrFe_{11}Zn_{0.5}Ni_{0.5}O_{19}$ ($SrFe_{12}O_{19}/NiFe_2O_4/ZnFe_2O_4$) nanoparticles having super paramagnetic nature are synthesized by co-precipitation of chloride salts using 7.5 M sodium hydroxide solution. The resulting precursors are heat treated (HT) at 900 and 1200 °C for 4 h in nitrogen atmosphere. During heat treatment, transformation proceeds as a constant rate of nucleation and three dimensional growth with an activation energy of 176.79 kJ/mol. The hysteresis loops show an increase in saturation magnetization from 1.042 to 59.789 emu/g with increasing HT temperatures. The 'as-synthesized' particles with spherical and needle shapes have size in the range of 20–25 nm. Further, these spherical and needle shaped nanoparticles tend to change their morphology to hexagonal plate and pyramidal shapes with increase in HT temperatures. The effect of such a systematic morphological transformation of nanoparticles on dielectric (complex permittivity and permeability) and microwave absorption properties are estimated in X band (8.2–12.2 GHz). The maximum reflection loss of the composite reaches −29.62 dB (99% power attenuation) at 10.21 GHz which suits its application in RADAR absorbing materials.

Keywords: A. Drying; B. Nanocomposites; C. Dielectric properties; D. Ferrites

1. Introduction

M type strontium hexaferrite ($SrFe_{12}O_{19}$), which is a hard hexagonal magnetic material, has been a subject of continuous interest for several decades due to its applicability in electronic components, magnetic memories and recording media [1]. The practical application of strontium hexaferrite as a permanent magnet is well known and it is also used as a dielectric or magnetic filler in the electromagnetic filler attenuation materials (EAM). EAM are used to minimize the electromagnetic interference (EMI), a specific type of environmental pollution which is caused by the extensive use of electromagnetic (EM) waves in wireless communications such as EM waves of 0.8–1.2 GHz are used for mobile phones, 2.45 GHz for electronic ranges, 5.6–8.2 GHz (G-band) for synthetic aperture radar (SAR) or microwave communication on the ground, 8.2–12.4 GHz (X-band) and 12.4–18 (Ku-band) for SAR or electron spin resonance (ESR) apparatus [2]. To overcome EMI problems, it is suggested that EM wave absorbing materials with capability of absorbing unwanted electromagnetic signals are to be used. Recently, the research pursuing to the development of various EM wave absorbers has been given much attention. Single material cannot meet these demands such as large absorption peak, wide working frequency range and thin absorption layer. In order to improve electromagnetic absorption properties of magnetic materials, new systems have been evolved comprising composite powder including hard and soft magnetic materials [3–5]. Nickel ferrite ($NiFe_2O_4$) and zinc ferrite ($ZnFe_2O_4$) having a cubic spinel structures are soft magnetic materials and are widely studied as microwave absorbing materials [6–8].

In view of this, in the present research, the microwave absorption properties of the composite powder consisting of hard magnetic strontium hexaferrite and soft magnetic nickel and zinc ferrite are studied.

* Corresponding author. Tel.: +91 01332 285739; fax: +91 01332 285243.
E-mail addresses: tyagidmt@iitr.ernet.in, matsachin@gmail.com (S. Tyagi).

0272-8842/$36.00
doi:10.1016/j.ceramint.2011.04.012

The conventional way of synthesizing hexaferrites involves solid state reaction route at high heat treatment (HT) temperature (≥1200 °C), which results in powders with large particle size, limited chemical homogeneity and low sinterability [9]. So, the preparation of fine and uniform hexaferrite powder without impurity is a challenging task. There are several other processing routes available in the literature [9–13]. Hydrothermal method employs expensive autoclaves, good quality seeds of a fair size and the impossibility of observing the crystal as it grows [14]. Sonochemical synthesis can generate a transient localized hot zone with extremely high temperature gradient and pressure [15] which can assist the destruction of the sonochemical precursor and the formation of nanoparticles. Low temperature combustion synthesis is complex, takes long time for self ignition reaction to occur and needs cationic surfactants to remove the impurity like hematite phase (αFe_2O_3) [16,17]. Mechanical alloying leads to impurity and lattice strains [9]. The present investigation deals with the synthesis of nickel and zinc substituted strontium hexaferrite nanoparticles by modified flux method. This method is economical and is quite suitable for mass production as compared to the other mentioned methods [18]. Further, reaction kinetics for the synthesis of nickel and zinc substituted strontium hexaferrite nanoparticles has been studied through examination of differential scanning calorimetry (DSC) data with various heating rates (10, 30 and 50 K/min). Activation energy has been obtained using non-isothermal method and '*n*' kinetic parameter has been obtained using Johnson–Mehl–Avrami (JMA) equation for analysis of the reaction in the formation of $SrFe_{11}Zn_{0.5}Ni_{0.5}O_{19}$. The studies on relative complex permittivity and permeability of nickel and zinc substituted strontium hexaferrite and their influence on microwave absorption properties are also carried out.

2. Experimental procedure

In the present study, analytical grades of ferric chloride ($FeCl_3{\cdot}6H_2O$), strontium chloride ($SrCl_2$), nickel chloride ($NiCl_2$), zinc chloride ($ZnCl_2$) and NaOH were used for synthesizing $SrFe_{11}Zn_{0.5}Ni_{0.5}O_{19}$ nanoparticles by modified flux method. Stoichiometric amounts of strontium chloride, nickel chloride and zinc chloride were dissolved completely into ultra pure water to make an aqueous solution (I). Ferric chloride was separately mixed in ultra pure water to make another aqueous solution (II). Both the above solutions were mixed in a 1:1 molar ratio. The brownish colored ferrite particles were precipitated from this mixture by gradually adding sodium hydroxide, NaOH (7.5 M) solution at room temperature (pH 12.0). The aqueous suspension was stirred gently for 15 min to achieve chemical homogeneity. The precipitates so formed were filtered off, washed with water and dried at 100 °C overnight. The precipitated nanocrystalline powder was mixed thoroughly with NaCl in 1:2 ratios (by weight). Since the melting point of NaCl is about 800 °C, so the 'as synthesized' particles were given a heat treatment of 900 and 1200 °C for 4 h in nitrogen atmosphere to achieve a uniform growth. During annealing, there was liquid phase diffusion of particles surrounding the molten NaCl salt which makes the process fast and hexaferrite particles crystallize out completely with uniform morphology after cooling in the furnace. The cooled mixture of nanoparticles and NaCl was then washed by ultra pure water. NaCl was dissolved and $SrFe_{11}Zn_{0.5}Ni_{0.5}O_{19}$ nanoparticles were filtered out.

3. Characterization studies

Reaction kinetics for the formation of nickel and zinc substituted strontium hexaferrite nanoparticles was studied in nitrogen atmosphere by differential scanning calorimetry, DSC (Perkin Elmer, Pyris Diamond) with various heating rates (10, 30 and 50 K/min). Phase identification of annealed samples was done by X-ray diffraction (XRD) using Bruker AXS D8 differactometer with Cu-Kα radiation. The average crystallite size of the powder was measured by X-ray line broadening technique employing Scherrer's formula. Morphological study was carried out by field emission scanning electron microscope, FESEM (QUANTA FEG 200 FEI) and transmission electron microscope, TEM (Philips, EM 400; TECHNAI 20G2-S-TWIN). Magnetic measurements were taken out at room temperature in the applied field range of −10000 to +10000 gauss using vibrating sample magnetometer, VSM (155, PAR). To study the dielectric properties, the nanoparticles (80 wt.%) were mixed with epoxy resin and 2% hardener. The ferrite epoxy composite thus obtained was cast into a rectangular pellet of thickness 2.5 mm and cured at 75 °C for 30 min. The composite thus prepared was polished and mounted on an aluminum foil (to obtain a single layer metal-backed absorber) to exactly fit into the measuring wave guide. The complex permittivity and permeability measurements were carried out on Network Analyzer (Agilent E8364B PNA series) using material measurement software 85071 in the frequency range of 8.2–12.2 GHz at room temperature. The reflection loss curves were calculated from complex permittivity and permeability at given frequency and absorber thickness with following equations:

$$Z_{in} = Z_0 \left(\frac{\mu_r}{\varepsilon_r}\right)^{1/2} \tanh\left\{ j\left(\frac{2\pi fd}{c}\right)(\mu_r\varepsilon_r)^{1/2}\right\}$$

$$RL = 20\log\left|\frac{Z_{in}-Z_0}{Z_{in}+Z_0}\right|$$

where f is the frequency, d is the thickness of absorber (d = 2.5 mm), c is the velocity of light, Z_{in} is the characteristic impedance of absorber and Z_0 is the characteristic impedance in a vacuum, $Z_0 = 120\pi$. The impedance matching condition is given by $Z_{in} = Z_0$ to represent the perfect absorbing properties.

3.1. Theoretical background for reaction kinetic study

The reaction rate of solid state transformation obeying JMA kinetic model can be written in the following form [19]

$$\frac{d\alpha}{dt} = An(1-\alpha)\left[\frac{\ln 1}{1-\alpha}^{(n-1/n)} \exp\left(\frac{-E}{RT}\right)\right] \quad (1)$$

where α is the reacted fraction, t is time for transformation, T is the absolute temperature, R is the gas constant = 8.314 J/mol/K, n is Avrami index parameter depending on the nucleation

mechanism and number of growth dimension, E is the activation energy, A is the pre exponent factor. The above equation is differentiated and equated to zero ($d^2\alpha/dt^2 = 0$) for maximum reaction rate at T_m temperature to obtain final equation as follows

$$\frac{\ln \beta}{T^2} = \frac{-E}{RT_m} + C_1 \quad (2)$$

where β is the heating rate, T_m is maximum reaction rate point, C_1 is a constant.

For all the different heating rates T_m is calculated from the DSC plots with the assumption that the peak of respective DSC plot for a particular heating rate (β) is maximum reaction rate point. The plot for $\ln \beta/T^2_m$ versus $1/T_m$ is linear and slope of this curve gives the activation energy E.

Integrating Eq. (1) and taking double natural logarithm and using Doyle's approximation [20].

$$\ln\left[\ln\left(\frac{1}{1-\alpha}\right)\right] = C_2 - 1.05\frac{nE}{RT} \quad (3)$$

where C_2 is a constant.

Thus, slope of the $\ln[\ln(1/1-\alpha)]$ versus $1/T$ plot gives the value of nE. Ratio of slopes of this plot and E (slope of plot for $\ln \beta/T^2_m$ versus $1/T_m$) would thus give value of 'n' for the reaction under a particular heating rate.

4. Results and discussion

The differential scanning calorimetry (DSC), differential thermogravimetry (DTG) and thermogravimetry (TG) traces of the samples carried out at the heating rates of 10, 30 and 50 K/min in nitrogen atmosphere are shown in Figs. 1–3 respectively. In all the three cases only endothermic peaks are observed indicating that nickel and zinc substituted strontium hexaferrite nanoparticles are formed by the endothermic reaction. The endothermic peak at about 814 °C (Fig. 1) is attributed to the synthesis of various phases like αFe_2O_3, $NiFe_2O_4$, $ZnFe_2O_4$ and $SrFe_{12}O_{19}$ which is confirmed by the XRD analysis of the powder heat treated at 900 °C in the nitrogen atmosphere (Fig. 4). The second endothermic peak at 1119 °C is attributed to endothermic reaction resulting in the synthesis of desired phases ($SrFe_{12}O_{19}$, $NiFe_2O_4$ and $ZnFe_2O_4$) with increasing crystallinity and is also confirmed by the XRD analysis of the powder heat treated at1200 °C in nitrogen atmosphere (Fig. 4). TG analysis of 'as synthesized' powder (Fig. 1) shows a weight loss of ~57% in the temperature range of 46–1123 °C. It may be due to degassing, loss of moisture and removal of NaCl during the heat treatment process. Thereafter no weight loss is observed. The differential thermogravimetry (DTG) curve indicates the derivative of themogravimetry data which is attributed to the rate of weight loss during the endothermic reactions occurring at 814 and 1119 °C (for the DSC carried out at 10 K/min). The endothermic reaction occurring at 1119 °C shows the weight loss of about 43.2% at the rate of 0.984 mg/min (shown by DTG curve). Thereafter both TG and DTG curves become smoother; this indicates the completion of reaction as M type strontium hexaferrite ($SrFe_{12}O_{19}$) with nickel and zinc ferrite ($NiFe_2O_4/ZnFe_2O_4$) is formed. The same behaviour is observed for the 'as synthesized' powder carried out under DSC/DTG/TG at 30 and 50 K/min with slight change

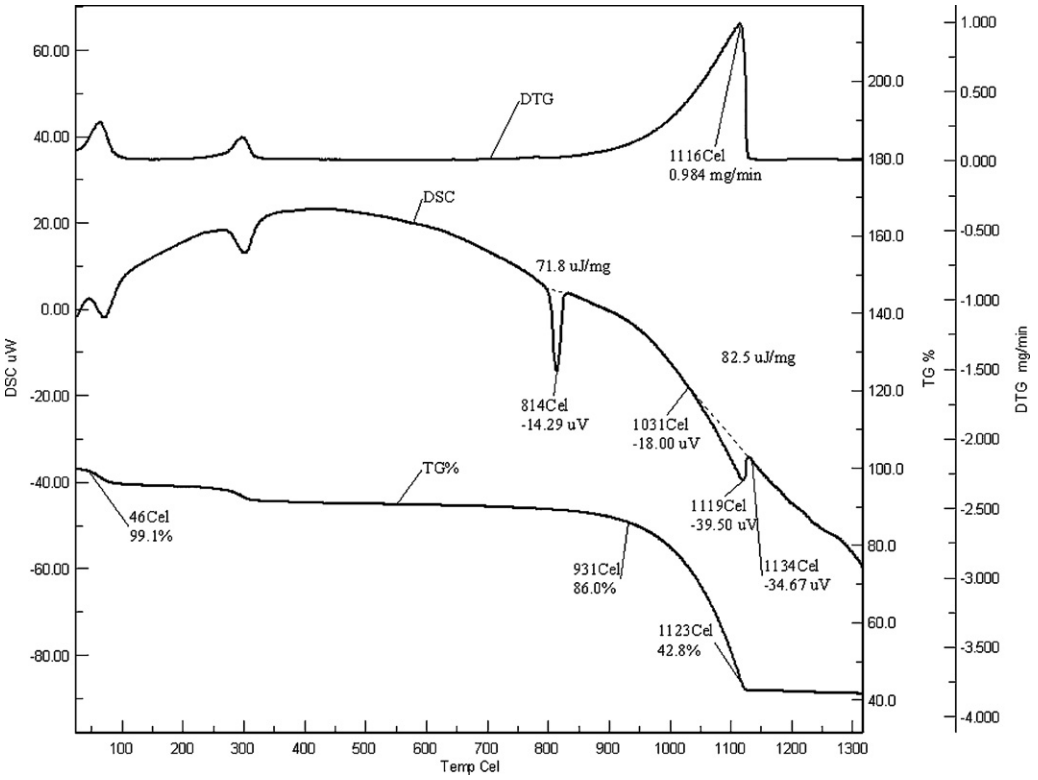

Fig. 1. DSC–DTG–TG traces of 'as synthesized' $SrFe_{12}O_{19}/NiFe_2O_4/ZnFe_2O_4$ nanoparticles at 10 K/min in nitrogen atmosphere.

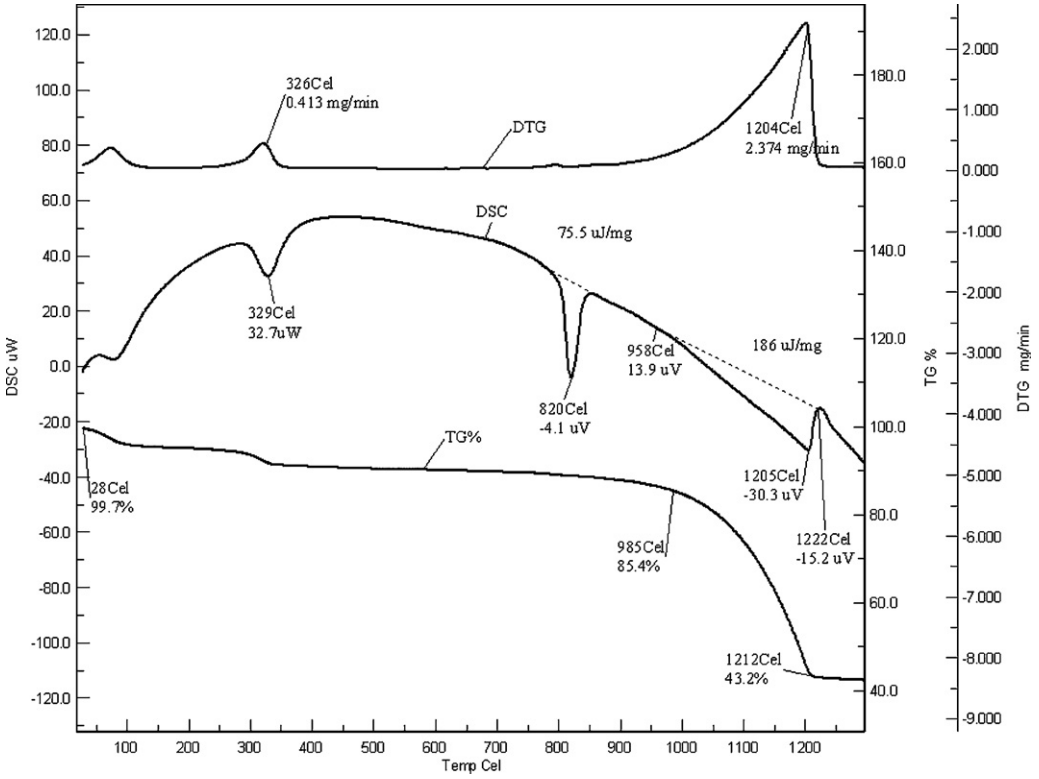

Fig. 2. DSC–DTG–TG traces of 'as synthesized' $SrFe_{12}O_{19}/NiFe_2O_4/ZnFe_2O_4$ nanoparticles at 30 K/min in nitrogen atmosphere.

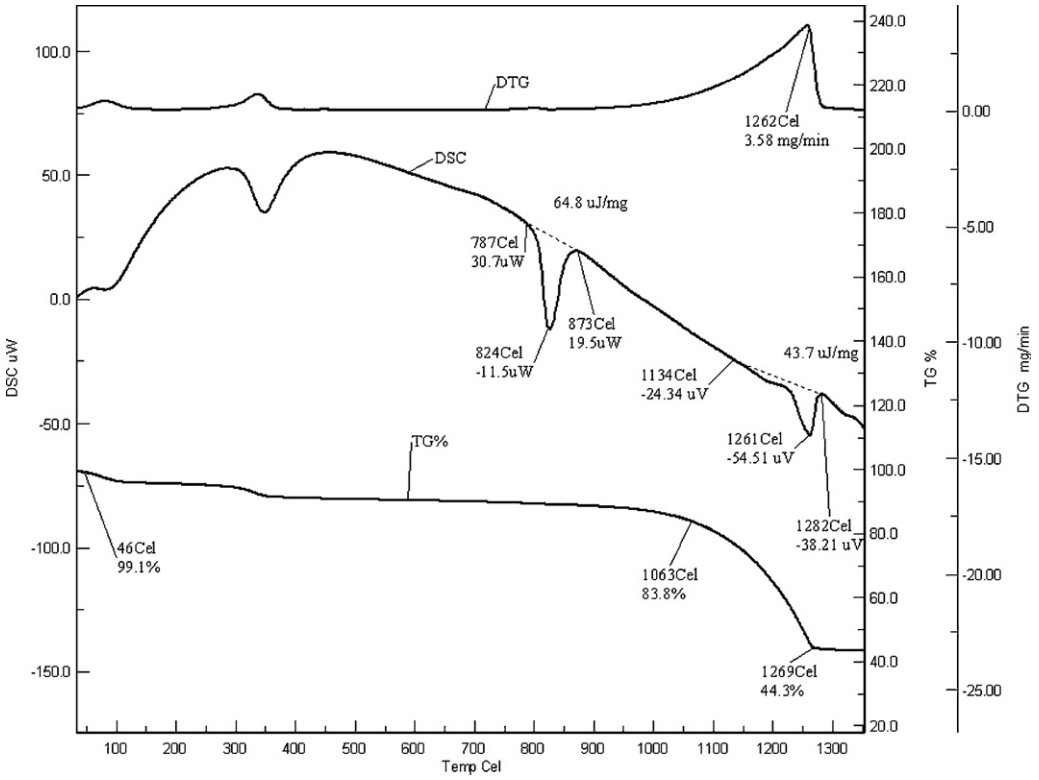

Fig. 3. DSC–DTG–TG traces of 'as synthesized' $SrFe_{12}O_{19}/NiFe_2O_4/ZnFe_2O_4$ nanoparticles at 50 K/min in nitrogen atmosphere.

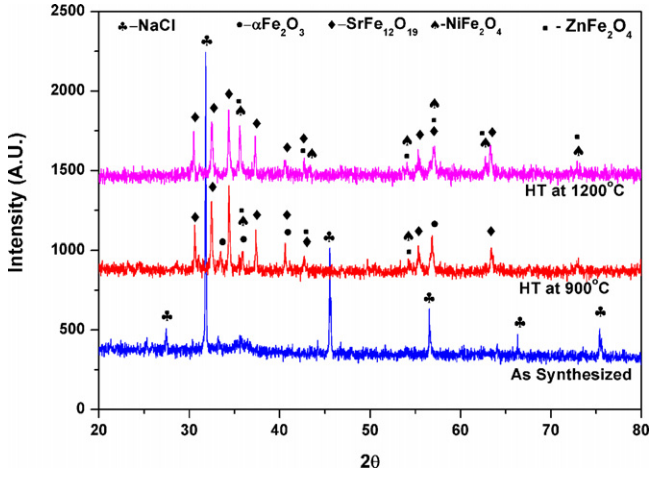

Fig. 4. XRD pattern of $SrFe_{12}O_{19}/NiFe_2O_4/ZnFe_2O_4$ nanoparticles in 'as synthesized' and heat treated at 900 and1200 °C in nitrogen atmosphere.

in the temperature of the reaction (Figs. 2–3). For the final reaction, the area under the DSC curve (enthalpy of reaction) and T_m (temperature of reaction) for various heating rates (10, 30 and 50 K/min) is given in Table 1. Hence the present investigation contributes towards the selection of heat treatment temperature, proper heating rate and required atmosphere for synthesizing $SrFe_{12}O_{19}/NiFe_2O_4/ZnFe_2O_4$ nanoparticles.

The indexed XRD patterns of the $SrFe_{12}O_{19}/NiFe_2O_4/ZnFe_2O_4$ nanoparticles in 'as synthesized' and after heat treatment at 900 and 1200 °C for 4 h in the nitrogen atmosphere are shown in Fig. 4. From the results, it can be inferred that the ferrite powder in 'as synthesized' condition is showing only the peak corresponding to impurity of NaCl (JCPDS 5-637). When annealed at 900 °C, $SrFe_{12}O_{19}$, $2\theta = 34.386$ (JCPDS 24-1207), $NiFe_2O_4$, $2\theta = 35.710$ (JCPDS 3-875) and $ZnFe_2O_4$, $2\theta = 35.542$ (JCPDS 02-1043) were obtained along with other phase correspond to impurity of αFe_2O_3 (JCPDS 05-637). As expected, the degree of crystallinity and amount of $SrFe_{12}O_{19}/NiFe_2O_4/ZnFe_2O_4$ nanoparticles are further increased by increasing the heat treatment temperature from 900 to 1200 °C. The degree of crystallinity for the peak corresponding to the phases $NiFe_2O_4$ and $ZnFe_2O_4$ is 25% at 900 °C and it increases to 67% at 1200 °C. The crystallite size of $SrFe_{12}O_{19}$ phase ($2\theta = 34.386$) is found to increase with increase in heat treatment temperature. It increases from 50 nm at 900 °C to 55 nm at 1200 °C. From the XRD and DSC results, it is concluded that under the given co-precipitation reaction, the ferric chloride is converted to $\alpha Fe(OH)_3$ and NaCl, which is then dehydrated to form αFe_2O_3. Nickel chloride is converted to $Ni(OH)_2$ and NaCl which further dehydrated to nickel oxide.

Table 1
Area under DSC curve (enthalpy) and T_m for various heating rates.

Heating rate (K/min)	T_m (K)	Enthalpy (μJ/mg)
10	1392	82.5
30	1478	186
50	1534	43.7

Zinc chloride is converted to $Zn(OH)_2$ and NaCl which further dehydrated to zinc oxide; and strontium chloride is also dehydrated to $Sr(OH)_2$ which further converted to strontium oxide. Finally, $SrFe_{12}O_{19}/NiFe_2O_4/ZnFe_2O_4$ nanoparticles are formed during the post synthesis calcinations stage and can be described by the following chemical reactions.

Neutralization with sodium hydroxide

$$12FeCl_3 + 36NaOH \rightarrow 12Fe(OH)_3 + 36NaCl$$

$$NiCl_2 + 2NaOH \rightarrow Ni(OH)_2 + 2NaCl$$

$$ZnCl_2 + 2NaOH \rightarrow Zn(OH)_2 + 2NaCl$$

$$SrCl_2 + 2NaOH \rightarrow Sr(OH)_2 + 2NaCl$$

Nucleation of nano crystals

$$12Fe(OH)_3 \rightarrow 6Fe_2O_3 + 18H_2O$$

$$Ni(OH)_2 \rightarrow NiO + H_2O$$

$$Zn(OH)_2 \rightarrow ZnO + H_2O$$

$$Sr(OH)_2 \rightarrow SrO + H_2O$$

Growth of nano crystals

$$NiO + Fe_2O_3 \rightarrow NiFe_2O_4$$

$$ZnO + Fe_2O_3 \rightarrow ZnFe_2O_4$$

$$SrO + 6Fe_2O_3 \rightarrow SrFe_{12}O_{19}$$

Using the non-isothermal kinetics as per Eq. (2), plot of $\ln \beta/T^2_m$ versus $1/T$ is obtained as shown in Fig. 5. From the slope of this curve, the activation energy (E) for the reaction is calculated to be 176.79 kJ/mol. Value of n is evaluated from $\ln[\ln 1/(1-\alpha)]$ versus $1/T$ plots based on the relationship depicted in Eq. (3). These plots are indicated in Fig. 6 for the reaction occurring at heating rates of 10 K/min, 30 K/min and 50 K/min in nitrogen atmosphere respectively. The n values are obtained from the slopes of these curves as shown in Fig. 6. The

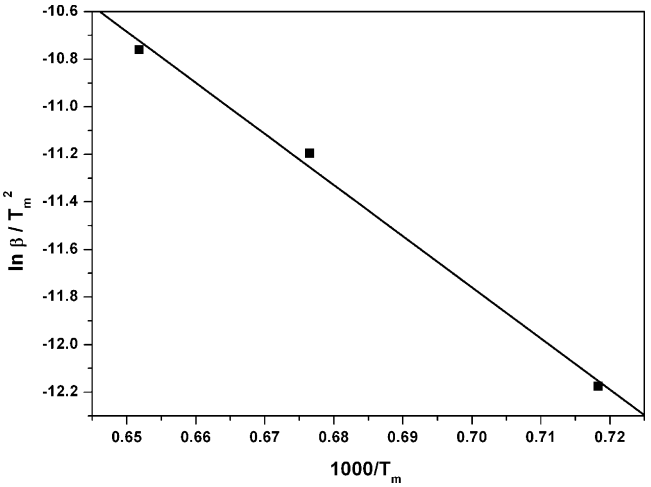

Fig. 5. Plot of $\ln \beta/T^2_m$ versus $1/T$ obtained for three heating rates 10, 30 and 50 K/min.

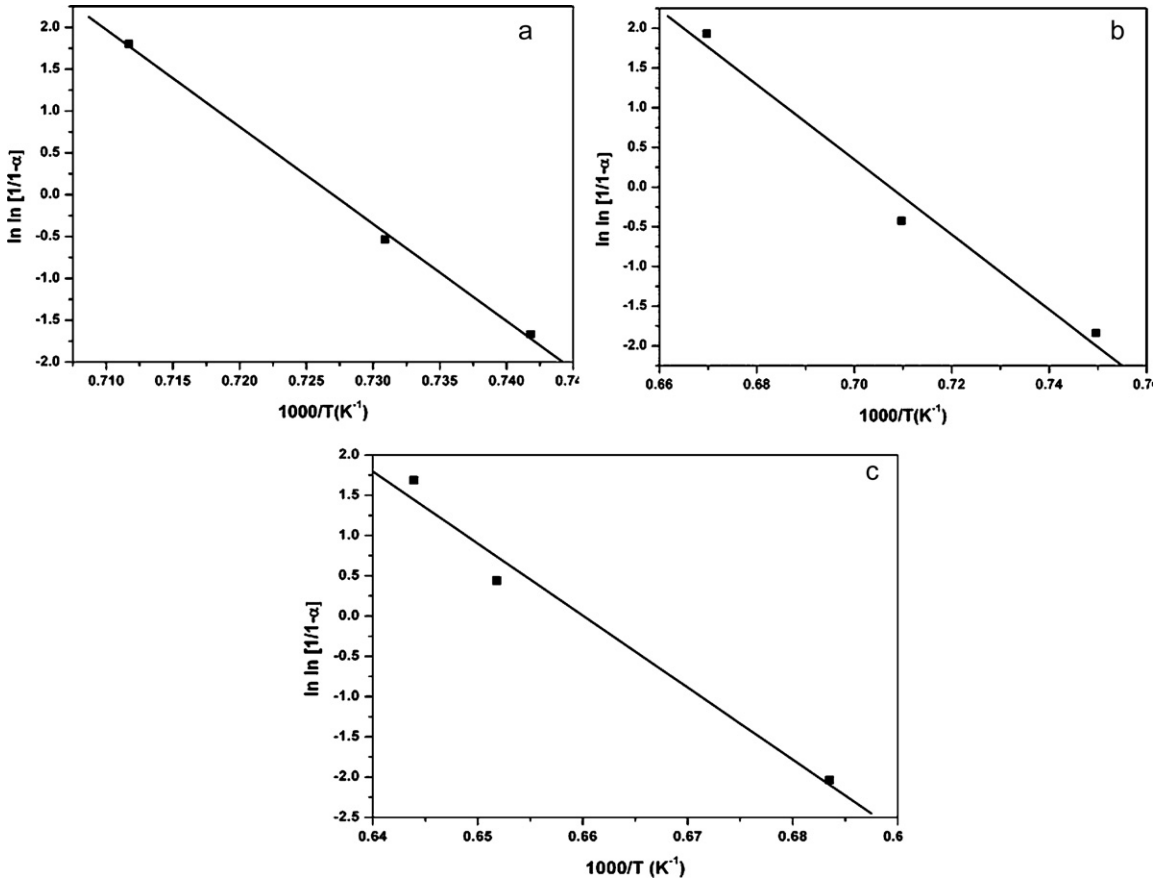

Fig. 6. Plot of ln[ln 1/(1 − α)] versus 1/*T* plots obtained for hexaferrites reaction at different rates, (a) 10 K/min, (b) 30 K/min, and (c) 50 K/min

value of Avrami exponent (*n*) is computed by dividing this slope by activation energy and is given in Table 2. The calculated values of Avrami exponent are found to be in the range of 4.191–4.461 for the formation of $SrFe_{12}O_{19}$/$NiFe_2O_4$/$ZnFe_2O_4$ nanoparticles. Based on Avrami exponent values (*n*), the mechanism for these reactions can thus be termed as, constant rate of nucleation and three-dimensional growth [19,20]. The values of activation energy and Avrami exponent are higher than those reported for single phase strontium hexaferrite [21]. The growth of multiple kinds of phases ($SrFe_{12}O_{19}$, $NiFe_2O_4$ and $ZnFe_2O_4$) can be restrained by each other, which leads to higher value of activation energy.

The FESEM micrographs of 'as-synthesized' and heat treated ferrite powders at temperatures of 900 and 1200 °C are shown in Fig. 7. In the 'as-synthesized' condition, the particles seem to have spherical and needle shaped morphology with particle size in the range of 20–25 nm (Fig. 7a). With increasing heat treatment temperature, the particles grow and constitute multiple morphologies. Also, with rise in heat treatment temperature, the systematic growth of particles is observed with sharp plane of crystals. This process of crystal growth and morphological evolution can be described in terms of Ostwald ripening. As the HT temperature is increased, these nanoparticles slowly disappear except for the few that grow larger, at the expense of smaller ones. Thus particles of small size act as nutrients for the bigger ones. At 1200 °C, $SrFe_{12}O_{19}$/$NiFe_2O_4$/$ZnFe_2O_4$ nanoparticles (with size in the range of 85–90 nm) having hexagonal plate and pyramidal shapes are observed (Fig. 7 and c). This is also evidenced by TEM micrograph of the powder in 'as-synthesized' and heat treated condition (Fig. 8). These multiple morphologies, possessing high surface areas, lead to plenty of interfacial polarization to weaken the energy of EM waves. It is reported that barium and strontium hexaferrite nanoparticles with hexagonal pyramidal and hexagonal plate like morphology are potential materials for the RADAR absorption applications [22–24].

Table 2
Slopes of ln[ln 1/1 − α] versus 1/*T* plots and calculated *n* values.

Heating rate (K/min)	Slope, *nE*/*R*	*n*
10	94.85×10^3	4.461
30	89.47×10^3	4.208
50	89.11×10^3	4.191

The magnetic measurements of $SrFe_{12}O_{19}$/$NiFe_2O_4$/$ZnFe_2O_4$ nanoparticles have almost negligible coercivity and remanance values (Fig. 9) in the 'as-synthesized' condition showing the superparamagnetic behaviour of the material. But when the 'as-synthesized' powders are heat treated at 900 and 1200 °C, the particles appear to transform from superparamagnetic to ferromagnetic nature. Saturation magnetization is found to be dependent on HT temperature. It increases from 1.042 to 59.789 emu/g with increase in HT temperature (Fig. 9). The rise in saturation magnetization with the HT

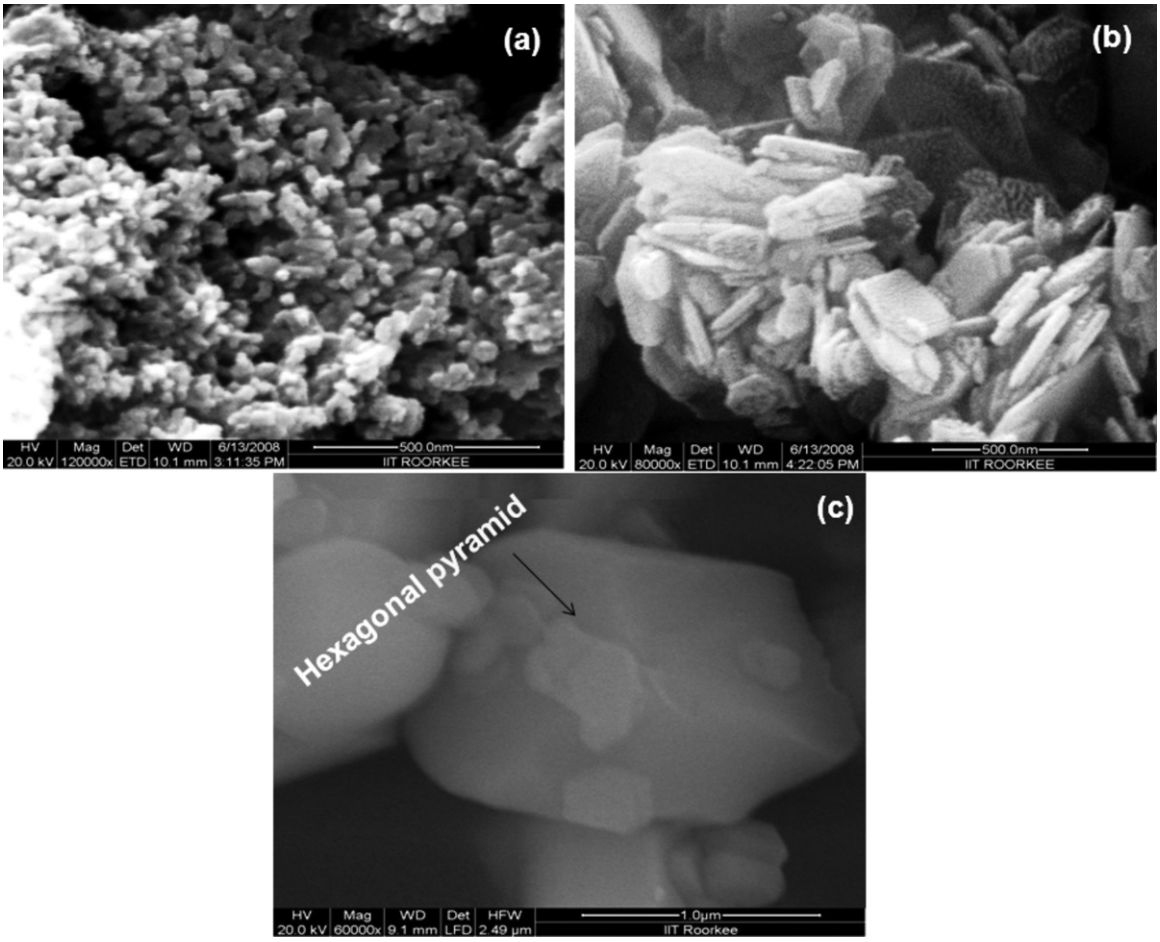

Fig. 7. FESEM micrographs showing the effect of heat treatment temperature on the morphology of $SrFe_{12}O_{19}/NiFe_2O_4/ZnFe_2O_4$ nanoparticles, (a) 'as synthesized' and heat treated at (b) 900 °C and (c) 1200 °C in nitrogen atmosphere.

temperature is attributed to the increased formation of strontium hexaferrite, zinc ferrite and nickel ferrite which is confirmed by X-ray study of powder HT at 1200 °C (Fig. 4) [18]. The coercivity of 2646 G is observed for the powder heat treated at 900 °C and thereafter decreases to 1274 G at 1200 °C. This might be due to the presence of αFe_2O_3 up to 900 °C; which has a high intrinsic coercive force [25]. Furthermore, the change in morphology and particle size affects the magnetic

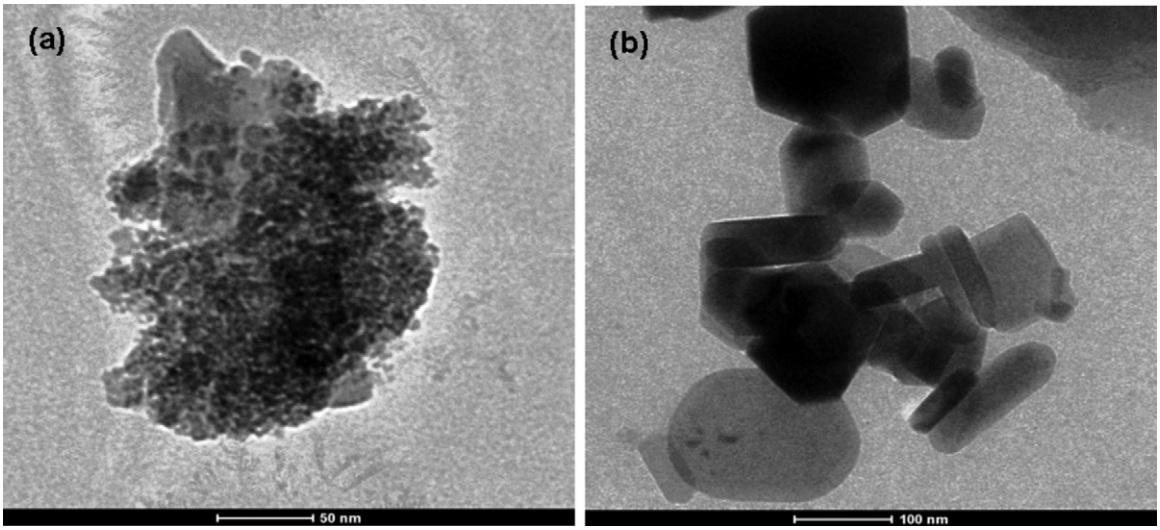

Fig. 8. TEM micrographs showing the effect of heat treatment temperature on the morphology of $SrFe_{12}O_{19}/NiFe_2O_4/ZnFe_2O_4$ nanoparticles, (a) 'as synthesized' and (b) heat treated at 1200 °C in nitrogen atmosphere.

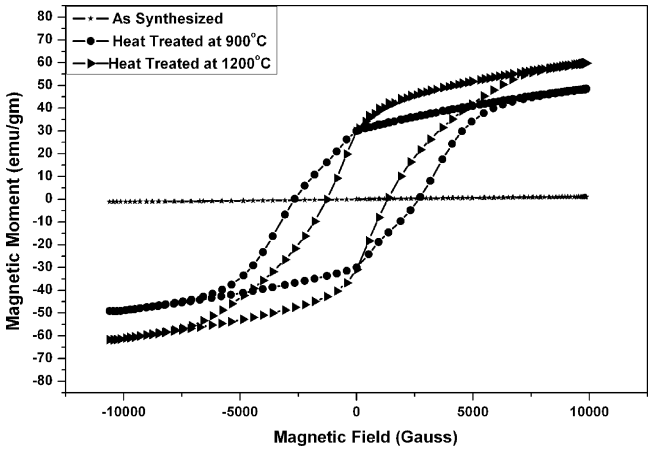

Fig. 9. The effect of HT temperature on hysteresis loops of $SrFe_{12}O_{19}/NiFe_2O_4/ZnFe_2O_4$ nanoparticles in 'as synthesized' condition and heat treated at 900 and 1200 °C in nitrogen atmosphere.

properties [18]. The co-precipitated powder heat treated with NaCl at 1200 °C having large hexagonal plate and pyramidal shape showed maximum saturation magnetization. While the co-precipitated powder heat treated with NaCl at 900 °C that have small hexagonal plate like structure in addition to αFe_2O_3 showed a maximum coercivity (Table 3). Thus the synthesis of spinel $NiFe_2O_4$, $ZnFe_2O_4$ along with hexagonal $SrFe_{12}O_{19}$ particles in nano size range results in higher saturation magnetization and lower coercivity than those reported for single phase strontium hexaferrite and nickel zinc ferrite [6,8,26]. Hexaferrite nanoparticles having low coercivity and high saturation magnetization find their applications in magnetic recordings in hard disks, floppy disks, video tapes, etc. [25].

Complex permittivity and permeability values represent the dielectric and magnetic properties of magnetic materials. The real parts (ε', μ') of complex permitivity and permeability symbolize the storage capability of electric and magnetic energy. The imaginary parts (ε'', μ'') represent the loss of electric and magnetic energy. As a microwave absorber, big imaginary parts of complex permittivity and permeability are expected. The real and imaginary parts of complex permittivity (Fig. 10a and b) and permeability (Fig. 11a and b) of nanoparticles are plotted as a function of frequency in X-band (8.2–12 GHz). It is observed that with the increase in heat treatment temperature from 'as-synthesized' condition to 1200 °C, both complex permittivity and permeability are observed to increase continuously. The real part of permittivity is found to increase from 5.646 (average value) in 'as synthesized' condition to 13.320 (average value) when heat treated at 1200 °C (Fig. 10a). The same trend is observed for the imaginary part of permittivity. The maximum imaginary permittivity of 6.627 (average value) is observed for the material heat treated at 1200 °C (Fig. 10b). Also, the real permeability increases from 1.157 (average value) in 'as-synthesized' condition to 1.291 (average value) when heat treated at 1200 °C (Fig. 11a). Similarly imaginary permeability

Table 3
Showing the effect of heat treatment temperature on the morphology and magnetic parameters of strontium hexaferrites.

Temperature (°C)	Morphology	Coercivity (G)	Remanance, M_r (emu/g)	Saturation magnetization, M_s (emu/g)	M_r/M_s
92 (as synthesized)	Spherical and needle (20–25 nm)	7.000	0.020	1.042	0.0200
900	Small hexagonal (70–75 nm)	2646	29.736	48.275	0.615
1200	Large hexagonal (85–90 nm)	1274	31.142	59.789	0.520

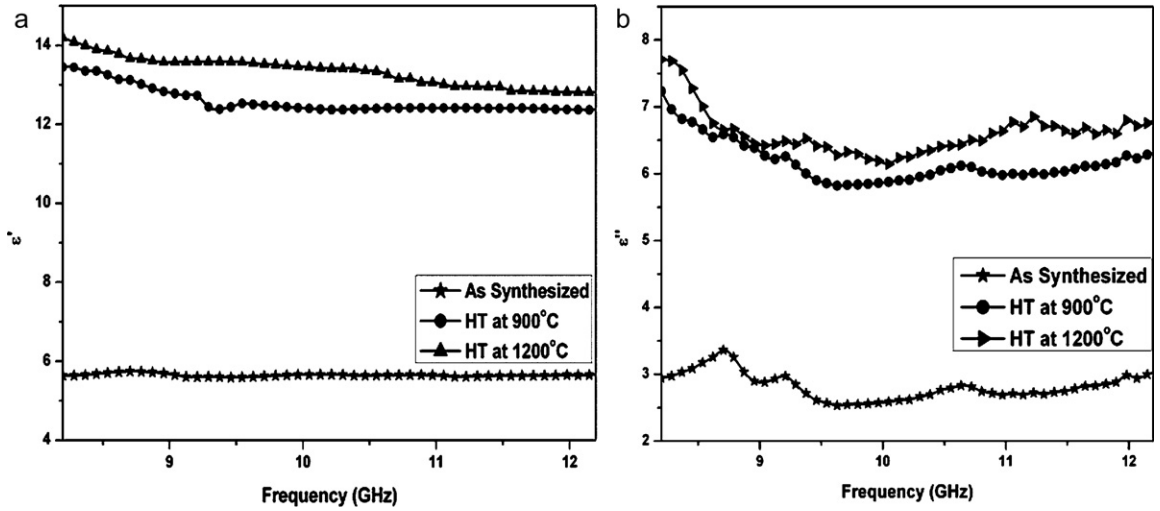

Fig. 10. The effect of HT temperature on real (ε') and imaginary (ε'') part of permitivity of $SrFe_{12}O_{19}/NiFe_2O_4/ZnFe_2O_4$ nanoparticles in 'as synthesized' condition and heat treated at 900 and 1200 °C in nitrogen atmosphere.

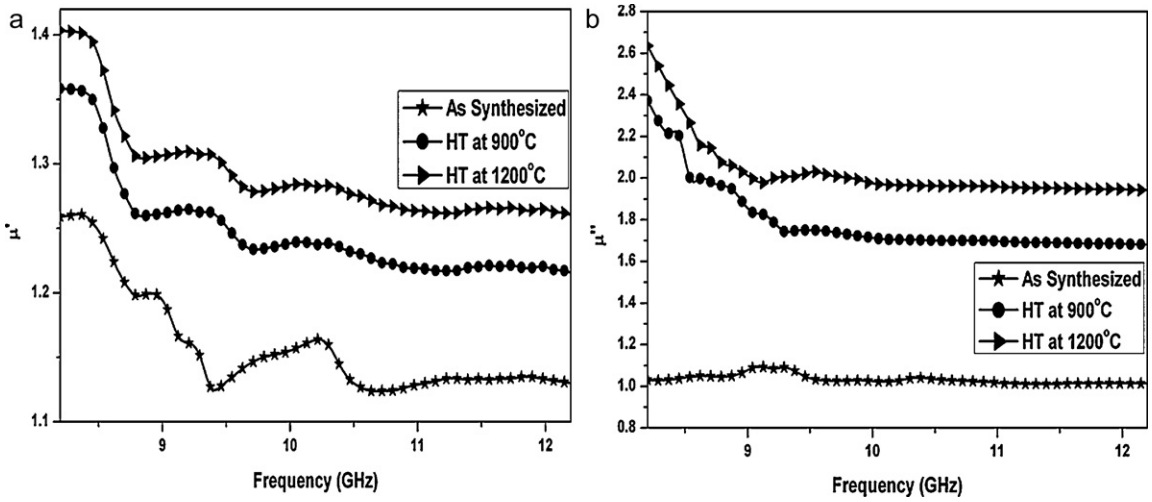

Fig. 11. The effect of HT temperature on real (μ') and imaginary (μ'') part of permeability of $SrFe_{12}O_{19}/NiFe_2O_4/ZnFe_2O_4$ nanoparticles in 'as synthesized' condition and heat treated at 900 and 1200 °C in nitrogen atmosphere.

is also increasing with increase in heat treatment temperature. The maximum imaginary permeability of 2.028 (average value) is observed for the powder heat treated at 1200 °C (Fig. 11b). The increase in complex permittivity and permeability with increase in heat treatment temperature in all the cases is attributed to the increased formation and growth of strontium hexaferrite and nickel zinc ferrite nanoparticles with increase in HT temperature. The significance of the results is the stability in the values of complex permittivity and permeability (obtained for large bandwidth) than those reported in literature [6–8,26,27] for pure strontium hexaferrite and nickel zinc ferrite.

The reflection losses (RL) for 'as-synthesized' $SrFe_{12}O_{19}/NiFe_2O_4/ZnFe_2O_4$ nanoparticles are low for all the frequencies between 8.2 and 12.2 GHz (Fig. 12) and minimum to maximum values are found to be in the range of −5.00 (at 8.2 GHz) to −15.20 B (at 10.21 GHz). For $SrFe_{12}O_{19}/NiFe_2O_4/ZnFe_2O_4$ nanoparticles heat treated at 900 °C, the reflection loss is evidently improved to −27.59 dB at 10.21 GHz and has further

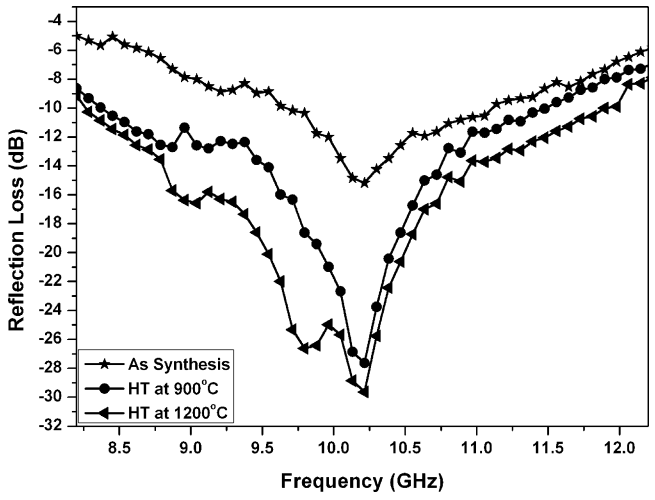

Fig. 12. The effect of HT temperature on reflection loss of $SrFe_{12}O_{19}/NiFe_2O_4/ZnFe_2O_4$ in 'as synthesized' condition and heat treated at 900 and 1200 °C.

enhanced to −29.62 dB for the material heat treated at 1200 °C (Fig. 12). The increment in reflection loss with increasing heat treatment temperature is attributed to the increased crystallization (Fig. 4) of $SrFe_{12}O_{19}/NiFe_2O_4/ZnFe_2O_4$ nanoparticles (crystallization effect). The strongest reflection loss and the widest bandwidths (for RL > 10 dB) are given in Table 4. The improvement of reflection loss originated from the formation of hard and soft ferrite which can be explained on the basis of exchange coupling interaction between hard magnetic ($SrFe_{12}O_{19}$) and soft magnetic ($NiFe_2O_4/ZnFe_2O_4$) phases, which changes the relative complex permeability of the materials. In this study, the nanocomposite powders are synthesized by modified flux method so three kinds of grains can be combined. The composite powder including hexaferrite ($SrFe_{12}O_{19}$) and spinel ferrite ($NiFe_2O_4/ZnFe_2O_4$) coupled to each other by exchange through interface of ferrite particles. There will be more interfaces if the grain size is smaller, and there will be stronger exchange coupling interaction at the interface. As we know, the cubic spinel crystal structure of $NiFe_2O_4/ZnFe_2O_4$ is similar to the structure of S-block of $SrFe_{12}O_{19}$, so it is possible that the vacancy of $NiFe_2O_4/ZnFe_2O_4$ is combined with Fe^{3+} at the $SrFe_{12}O_{19}$ surface, which is another possible reason for strong interface coupling interaction. Thus, exchange coupling interaction existing between hard and soft magnetic phases improves the dielectric and microwave absorption properties (interface effect) [4,5] which are in agreement with the present study. The size of particles heat-treated at 1200 °C (85–90 nm) is larger than that of particles heat-treated at 900 °C (70–75 nm). However, the strongest RL at 10.21 GHz for HT 1200 °C sample is −29.62 dB, which is larger than RL for HT at 900 °C. Obviously, there is a competition between interface effect and the crystallization effect on the reflection loss. Moreover, microwave absorption is enhanced, when the particle size is reduced from micron to nano size [28]. This can be explained on the basis of quantum size effect. In nanocrystallite particles, the quantum size effect makes the electronic energy levels split and the spacing between adjacent energy states increases

Table 4
Showing the strongest reflection loss and the widest bandwidths (for RL > 10 dB) in 'as synthesized' and heat treated conditions.

Powder	RL (dB) at 8.2 GHz	RL (dB) at 12.2 GHz	The widest bandwidth for RL > 10 dB (in GHz)	The strongest RL (dB) at 10.21 GHz
As synthesized	−5.00	−5.82	1.48 (9.62–11.10)	−15.20
HT at 900 °C	−8.63	−6.88	3.20 (8.36–11.56)	−27.59
HT at 1200 °C	−9.13	−8.28	3.70 (8.28–11.98)	−29.62

inversely with volume of the particles. If the particle of absorber medium is small enough and the discrete energy level spacing is in the energy range of microwave, the electron can absorb the energy as it transit from one level to another, and lead to increase in attenuation. The −10 dB absorption bandwidth corresponds to 68% EM wave amplitude attenuation or to 90% power attenuation, whereas a −20 dB absorption bandwidth corresponds to 90% amplitude attenuation or to 99% power attenuation [29]. The epoxy resin is an insulator and nonmagnetic; thus, it is transparent to EM waves. In the $SrFe_{12}O_{19}/NiFe_2O_4/ZnFe_2O_4$/epoxy composite, the epoxy resin only functions as matrix [29]. The reflection loss of the composite mainly stems from the contribution of $SrFe_{12}O_{19}/NiFe_2O_4/ZnFe_2O_4$ magnetic composite. Thus more than 99% power attenuation is observed for the composite material heat treated at 1200 °C which suits its application in Stealth defense in all military platforms.

5. Conclusions

(1) The hexagonal plate and pyramid shaped (85–90 nm) $SrFe_{12}O_{19}/NiFe_2O_4/ZnFe_2O_4$ nanoparticles are successfully synthesized for the powder heat treated at 1200 °C.
(2) The application of Johnson–Mehl–Avrami equation of the kinetics of endothermic reaction yielded overall empirical activation energy (E) of 176.79 kJ/mol for the synthesis of $SrFe_{12}O_{19}/NiFe_2O_4/ZnFe_2O_4$ nanoparticles during the calcinations.
(3) By Avrami exponent values (4.191–4.461), the mechanism for these reactions can thus be termed as, constant rate of nucleation and three-dimensional growth.
(4) The $SrFe_{12}O_{19}/NiFe_2O_4/ZnFe_2O_4$ nanoparticles show high value of saturation magnetization (59.789 emu/g) and low intrinsic coercivity (1274 G) when heat treated at 1200 °C as compared to powder heat treated at 900 °C (48.275 emu/g, 2646 G respectively)
(5) The real and imaginary parts of permittivity and permeability increase with increase in heat treatment temperature. The maximum reflection loss of −29.62 dB (99% power attenuation) at 10.21 GHz is obtained for the material heat treated at 1200 °C.

Acknowledgement

The authors acknowledge Ministry of Human Resource Development (MHRD), Government of India for the fellowship granted to first author of this study.

References

[1] B. Vishwanathan, V.R.K. Murthy, Ferrite Materials Science and Technology, Narosa Publishing House, New Delhi, 1990.
[2] D.S. Li, T. Horikawa, J.R. Liu, M. Itoh, K. Machida, Electromagnetic wave absorption properties of iron/rare earth oxide composites dispersed by amorphous carbon powder, J. Alloys Compd. 408 (2006) 1429–1433.
[3] O. Masala, D. Hoffman, N. Sundaram, K. Page, T. Proffen, G. Lawes, R. Seshadri, Preparation of magnetic spinel ferrite core/shell nanoparticles: soft ferrite on hard ferrites and vice versa, Solid State Sci. 8 (2006) 1015–1022.
[4] T. Maeda, S. Sugimoto, T. Kagotani, N. Tezuka, K. Inomata, Effect of soft/hard exchange interaction on natural resonance frequency and electromagnetic wave absorption of the rare earth–iron–boron compounds, J. Magn. Magn. Mater. 281 (2004) 195–205.
[5] J.R. Liu, M. Itoh, K.I. Machida, Magnetic and electromagnetic wave absorption properties of alpha-Fe/Z-type Ba-ferrite nanocomposites, Appl. Phys. Lett. 88 (2006) 1–3, 062503/.
[6] V. Sunny, P. Kurian, P. Mohanan, P.A. Joy, M.R. Anantharaman, A flexible microwave absorber based on nickel ferrite nanocomposite, J. Alloys Compd. 489 (2010) 297–303.
[7] T. Giannakopoulou, L. Kompotiatis, A. Kontogeorgakos, G. Kordas, Microwave behavior of ferrites prepared via sol–gel method, J. Magn. Magn. Mater. 246 (2002) 360–365.
[8] C.H. Peng, C.C. Hwang, J. Wan, J.S. Tsai, S.Y. Chen, Microwave-absorbing characteristics for the composites of thermal-plastic polyurethane (TPU)-bonded NiZn-ferrites prepared by combustion synthesis method, Mater. Sci. Eng. B 117 (2005) 27–36.
[9] B.D. Cullity, C.D. Graham, Introduction to Magnetic Materials, second ed., John Wiley & Sons, New Jersey, 2008.
[10] T.S. Chin, S.L. Hsu, M.C. Deng, Barium ferrite particulates prepared by salt-melt method, J. Magn. Magn. Mater. 120 (1993) 64–68.
[11] X. Liu, J. Wang, L.M. Gan, S.C. Ng, Improving the magnetic properties of hydrothermally synthesized barium ferrite, J. Magn. Magn. Mater. 195 (1999) 452–459.
[12] M. Sivakumar, A. Gedanken, W. Zhong, Y.W. Du, D. Bhattacharya, Y. Yeshurun, I. Felner, Nanophase formation of strontium hexaferrite fine powder by sonochemical method using $Fe(CO)_5$, J. Magn. Magn. Mater. 268 (2004) 95–104.
[13] J. Huang, H. Zhuang, W. Li, Optimization of the microstructure of low temperature combustion synthesized barium ferrite powder, J. Magn. Magn. Mater. 256 (2003) 390–395.
[14] M. O'Donoghue, A Guide to Man-made Gemstones, Van Nostrand Reinhold, Great Britain, 1983.
[15] K.S. Suslick, Ultrasound: Its Chemical, Physical and Biological Effects, VCH, Weinheim, 1988.
[16] M.G. Hasab, S.A.S. Ebrahimi, A. Badiei, An investigation on physical properties of strontium hexaferrite nanopowder synthesized by a sol–gel auto-combustion process with addition of cationic surfactant, J. Eur. Ceram. Soc. 27 (2007) 3637–3640.
[17] M.G. Hasab, S.A.S. Ebrahimi, A. Badiei, The effect of surfactant hydrocarbon tail length on the crystallite size of Sr-hexaferrite powders synthesized by a sol–gel autocombustion method, J. Eur. Ceram. Soc. 310 (2007) 2477–2479.

[18] M.M. Hessien, M.M. Rashad, K. El-Barawy, Controlling the composition and magnetic properties of strontium hexaferrite synthesized by co-precipitation method, J. Magn. Magn. Mater. 320 (2008) 336–343.
[19] J.M. Criado, A. Ortega, Non isothermal crystallization kinetics of metal glasses: simultaneous determination of both the activation energy and the exponent *n* of The JMA Kinetic Law, Acta Metall. 35 (1987) 1715–1721.
[20] C.D. Doyle, Estimating isothermal life from thermogravimetric data, J. Appl. Polym. Sci. 6 (1962) 639–642.
[21] S. Tyagi, R.C. Agarwala, V. Agarwala, Reaction kinetic studies of strontium hexaferrite nanoparticles synthesized by co-precipitation method, Trans. Ind. Inst. Met. 63 (63) (2010) 15–19.
[22] S. Tyagi, R.C. Agarwala, V. Agarwala, Microwave absorption and magnetic studies of strontium hexaferrite nanoparticles synthesized by modified flux method, J. Nano Res. 10 (2010) 19–27.
[23] R. Sharma, R.C. Agarwala, V. Agarwala, Development of RADAR absorbing nano crystals by microwave irradiation, Mater Lett. 62 (2008) 2233–2236.
[24] R. Sharma, R.C. Agarwala, V. Agarwala, Development of radar absorbing nano crystals under thermal irradiation, J. Nano Res. 2 (2008) 91–104.
[25] Y.P. Fu, C.H. Lin, Fe/Sr ratio effect on magnetic properties of strontium ferrite powders synthesized by microwave induced combustion process, J. Alloys Compd. 386 (2005) 222–227.
[26] A. Ataie, S. Heshmati-Manesh, Synthesis of ultra-fine particles of strontium hexaferrite by a modified co-precipitation method, J. Eur. Ceram. Soc. 21 (2001) 1951–1955.
[27] H. Zhao, X. Sun, C. Mao, J. Du, Preparation and microwave-absorbing properties of $NiFe_2O_4$–polystyrene composites, Physica B 404 (2009) 69–72.
[28] S. Ruan, B. Xu, H. Suo, F. Wu, S. Xiang, M. Zhao, Microwave absorptive behavior of ZnCo substituted W-type Ba hexaferrite nanocrystalline composite material, J. Magn. Magn. Mater. 212 (2000) 175–177.
[29] X. Liu, Z. Zhang, Y. Wu, Absorption properties of carbon black/silicon carbide microwave absorbers, Composites: Part B 42 (2011) 326–329.